Dynamic Beam-Stabilized, Additive-Printed Flexible Antenna Arrays with On-Chip ~~Fast~~ Rapid Insight Generation

Sreeni Poolakkal[1*], Abdullah Islam[2], Arpit Rao[1], Shrestha Bansal[1], Ted Dabrowski[3], Kalsi Kwan[3], Zhongxuan Wang[2], Amit Kumar Mishra[4], Julio Navarro[3], Shenqiang Ren[2], John Williams[3], Sudip Shekhar[4], Subhanshu Gupta[1]

[1]School of Electrical Engineering and Computer Sciences, Washington State University, 355 NE Spokane St, Pullman, 99163, WA, USA.
[2]Department of Materials Science and Engineering, University of Maryland, MD, USA.
[3]Additive Printing, Boeing, AL, USA.
[4]Department of Electrical and Computer Engineering, University of British Columbia, BC, Canada.

*Corresponding author(s). E-mail(s): sreeni.poolakkal@wsu.edu;

1 Supplementary Information

1.1 Environmentally Friendly Alternative for Conventional Subtractive Processes

While lightweight conformal arrays are convenient in many applications, large-scale production of these arrays raises major concerns over chemical waste and water pollution during fabrication. Various steps in the traditional subtractive process result in substantial chemical waste generation, including spent etchants, contaminated rinse water, filter sludges, and discarded chemicals. Spent etchant, a strong acid or base, is used to remove unwanted copper from PCBs. Plating bath wastewater is generated from the electroplating process used to deposit metal layers onto PCBs. Rinse water, used to rinse the PCBs after each fabrication step, contains a variety of acids and

bases. Most of these fabrication plants are situated near water sources and require substantial amounts of water for each step. This chemical waste can contaminate soil and water, posing serious environmental challenges.

Amid these concerns, additive printing, also known as 3D printing, is an appropriate solution for printed circuit fabrication, offering numerous advantages over conventional subtractive manufacturing methods. PCB design using additive printing does not require any chemical processing, as the entire circuit board can be printed using an inkjet printer. Additive printing requires only the material needed to create the PCB, significantly reducing waste and eliminating various chemical processes. Furthermore, additive printing allows for the creation of complex, thermally conductive structures within the PCB itself, improving the overall thermal performance of the array. While the initial investment in additive printing can be significant, the long-term cost benefits are substantial. The reduced material waste, fewer processing steps, and shorter development cycles translate to lower production costs over time.

1.2 Experimental Setup

The Dynamic Beam-Stabilized (DBS)-based Flexible Antenna Array (DBS-FLEX) requires two different experimental setups: (i) to verify ink stability and ink characteristics before additive printing antenna array, and (ii) to validate DBS-FLEX functionality under deformation.

To characterize the stability and Radio Frequency (RF) properties of the ink, a simple dipole antenna operating at 2.1 GHz is printed using the ink. As shown in Fig. 2, the dipole is subjected to varying strains, and its reflection coefficient S_{11} is measured. The dipole is designed with an origami feed line, allowing it to endure up to 30% strain. Similarly, another dipole antenna with a standard feed line, also operating at 2.1 GHz, is printed using the ink and subjected to different temperature conditions.

Figure 4a and b illustrates the test setup employed to validate the Beamforming Integrated Circuit (BFIC) and the proposed beam stabilization technique. The additive printed array, along with the BFIC, is mounted on the DAMS D6025 antenna measurement platform as shown in Fig. 4a. The signals are generated in MATLAB and transmitted through a Pasternack PE9887 horn antenna using Digital-to-Analog Converter (DAC) on Xilinx ZCU216 RFSoC. The high resolution DACs in ZCU216 allow transmission of signals from single tone to QAM modulated wideband signals (Fig. 4a). A 4.2 GHz differential clock is provided from ADF4372 EVM (wideband synthesizer) to the internal mixer and sampler clock generation circuit of the BFIC. The bias voltages for both the BFIC and the DBS are provided using a DAC81416 EVM. The serial control bits are sent to the on-chip serial to peripheral interface (SPI) registers from a Digilent Analog Discovery 2 board. The quadrature BF_{out} outputs post-combining from BFIC is captured on the Xilinx ZCU216 Analog-to-Digital Converter (ADC)s and subsequently converted to a 16-bit digital word using a mapping function. The digital BF_{out} is then fed to the calibration loop, interfaced through a Waveshare QFN-64 programmable adapter socket. After each iteration, the new control bits for each phase are captured from the respective calibration loops and updated to the serial control bit stream. This is then fed to the SPI control registers using the Digilent Analog Discovery 2. The entire data capture loop is automated

through the power automation tool [1].

1.3 Single tile 2 × 2 Receiver Array Performance

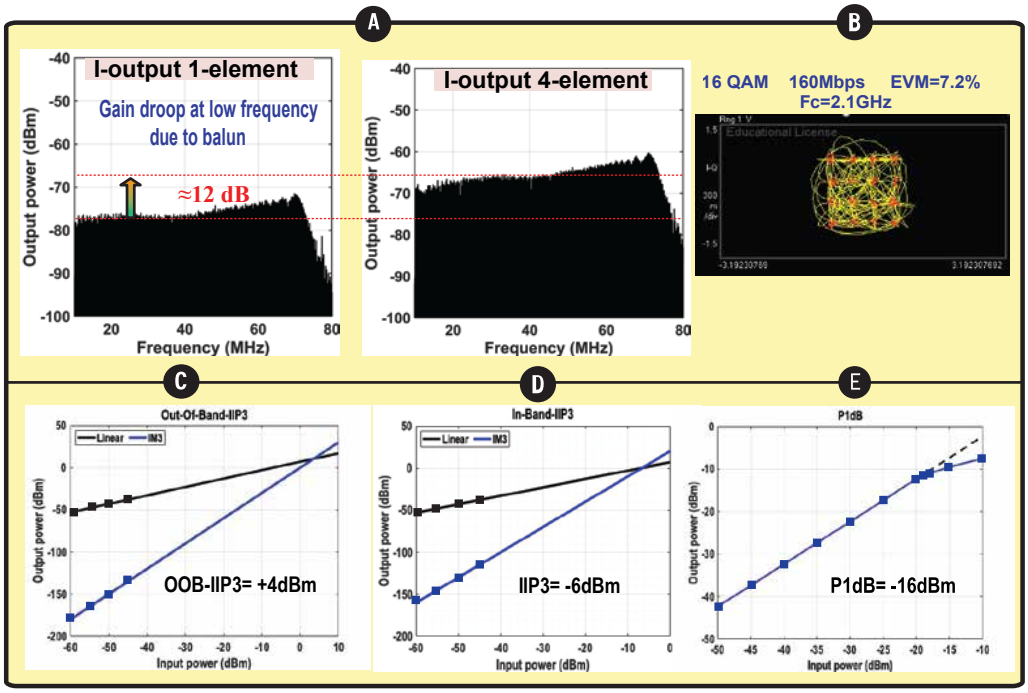

Supplementary Fig. 1 Measured BFIC performance including **a.** beamforming gain over wideband modulated input with 1-element and 4-element, **b.** EVM for 16-QAM modulation, **c.** out-of-band IIP3, **d.** in-band IIP3, and **e.** 1-dB compression point.

Supplementary Fig. 1a shows the wideband beamforming capabilities of the proposed receiver array. This measurement uses the same test bench shown in Fig. 4b. The wideband signal is generated in MATLAB and transmitted using ZCU216 DAC from the Pasternack PE9887 horn antenna at 0° angle. A ≈12 dB beamforming gain is observed when all four elements are enabled. The gain profile has a reduced gain at lower frequencies (for both 1-element and 4-element) due to the high-pass response of the ZCU216 ADC baluns connected at the BFIC output. The measured constellation plot in Supplementary Fig. 1b shows that the receiver supports 16-QAM modulation with an error vector magnitude (EVM) of 7.2% while supporting 160 Mbps data rate.

Supplementary Fig. 1c-e shows the linearity performance of a single-channel BFIC. The measured 1-dB compression point is -16 dBm, which is in reasonable agreement with the simulation results. The in-band IIP3 shown in Supplementary Fig. 1d is measured using a two-tone test where the first tone is placed at a frequency offset Δf from LO and the second tone at $2\Delta f - 5$ MHz offset from LO such that the IM3 product will fall at 5 MHz. Measured in-band IIP3 is -6 dBm for a gain setting of 7 dB. The out-of-band IIP3 shown in Supplementary Fig. 1d was also measured using a two-tone test with the first tone at an offset of 250 MHz from the LO and the second

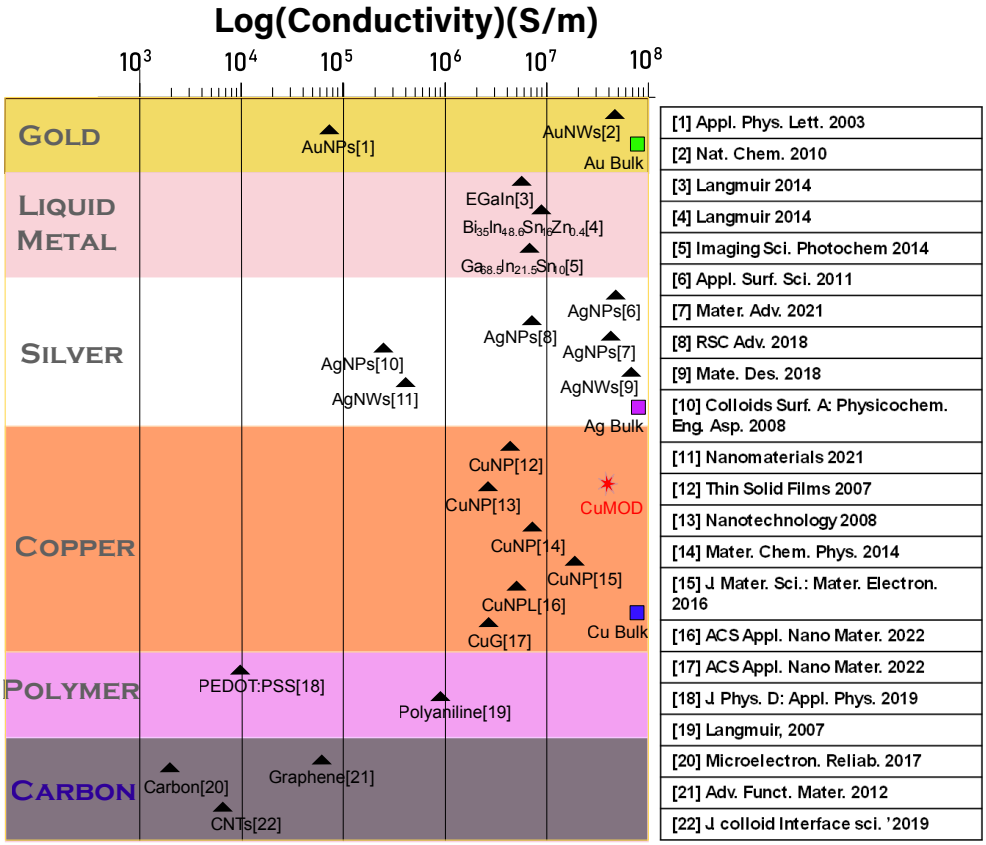

Supplementary Fig. 2 Comparative chart of the proposed Copper Molecular Decomposition (CuMOD) ink, providing electrical conductivity with state-of-the-art inks and bulk metals. References: AuNPs [2],AuNWs [3], EGain [4], $Bi_{35}In_{48.6}Sn_{16}Zn_{0.4}$ [4], $Ga_{68.5}In_{21.5}Sn_{10}$ [5], AgNPs [6–9], AgNW [10, 11], CuNPs [12–15], CuNPLs [12], CuG [12], Carbon [16], CNTs [17], Graphene [18], PEDOT:PSS [19], Polyaniline [20].

tone at 370 MHz offset from LO such that the IM3 distortion component will fall at 30 MHz. The measurement shows an increase in out-of-band-IIP3 from in-band-IIP3 as it reaches +4 dBm for a gain setting of 7 dB.

The power breakdown for the proposed BFIC is shown in Fig. 22, with the four RF front-end units consuming the highest power. The LNTA, passive mixer, TIA, and buffer, together with a few test circuits, consume 41 mW in total power. Clock drivers, LO Generation, LO PS, and sampler clock generation, together with the PI and the time-interleaved sample-and-hold clocking, consume 27 mW. The charge-domain summer, which includes a 2-stage internally compensated OTA, consumes 6 mW, including both the quadrature paths. The SPI registers only consume 26 μW. The 3-variable calibration loop consumes 4.5 mW.

Radiation pattern measurement uses the same test setup with the receiver array and is rotated from $-90°$ to $+90°$ using the DAMS D6025 (with 5° resolution) to capture the received power level at each angle. The receiver array is flipped 90° to

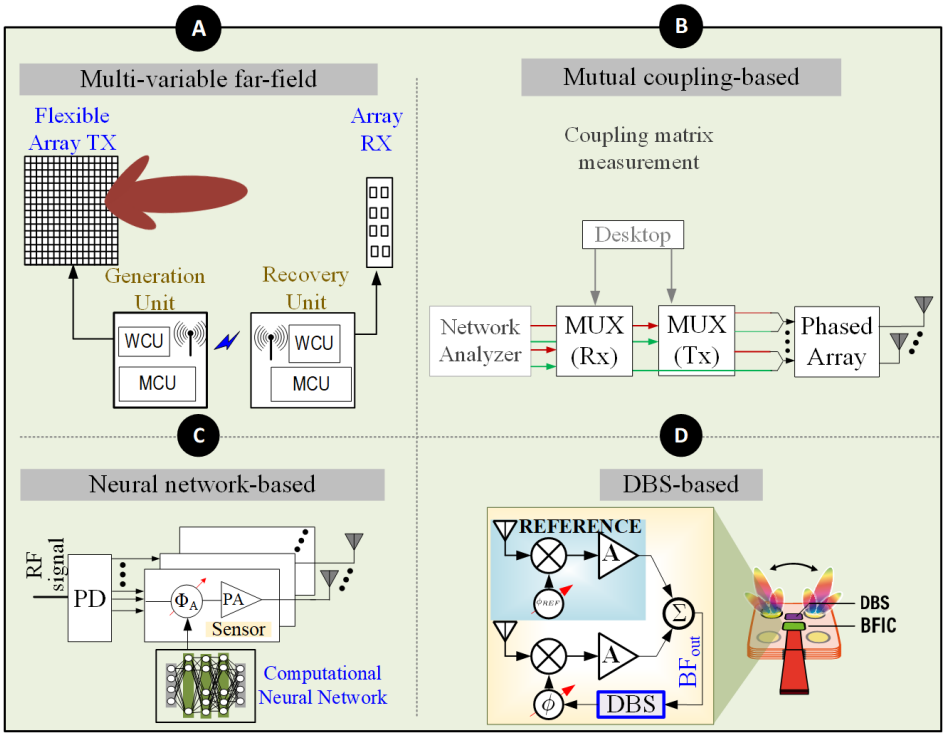

Supplementary Fig. 3 Various approaches in the state-of-the-art to correct deformation induced beam pointing error. **a.** FPGA-based algorithm supported by a wireless back propagation unit. **b.** Neural network-based pretrained deformation correction. **c.** Element-level mutual coupling sensing-based deformation correction. **d.** Proposed array level DBS based deformation correction. TX - transmitter, RX - receiver, WCU - Wireless Communication Unit, PD - Power Divider, and PA - Power Amplifier.

capture the radiation pattern in the elevation plane using the same test setup. Fig. 5c-d shows the azimuth and the elevation radiation patterns. The test setup limited measurement of the radiation pattern and efficacy deformation induced beam pointing error correction in an arbitrary plane ($El \neq 0°$ and $Az \neq 0°$).

1.4 State-of-the-Art comparison

CuMOD Ink: Supplementary Figure 2 illustrates the performance gap between various additive-manufacturable ink materials and bulk metals in terms of conductivity. Unlike prior art in gold, silver, carbon nanotubes, liquid metal, and conductive polymers, CuMOD ink significantly closes the conductivity gap.

DBS: Supplementary Fig. 3 shows various approaches for deformation-induced beam-pointing error. In [21] (Supplementary Fig. 3a), a multi-dimensional variable dynamic range search algorithm adjusts the array weights to stabilize the beam, but its higher computational complexity ($O(N^4)$) and parallelism demands costly field-programmable gate array (FPGA) architectures, besides the additional requirement

Table Supplement1 Resource utilization of Dynamic Beam Stabilization.

Multipliers	10
Adders/Subtractors	11
Registers	81 (1-bit) + 133 (16-bit)
Multiplexers	9

for separate generation and recovery units connected through a separate wireless back propagation link. Adapting this technique in airborne platoons and portable units is thus challenging. The pre-trained deep-learning-based beam stabilization technique presented in [22] (Supplementary Fig. 3b) relies heavily on training data with prior knowledge of the deformation, deformation surface, and operational environment. Under uncertain dynamic operational conditions, this technique fails to stabilize the beam. Furthermore, these models require periodic update and maintenance of multiple dictionary sets, demanding an exponential increase in memory storage as the array size is scaled. Element-level mutual coupling-based deformation measurement and compensation using an off-chip algorithm was demonstrated in [23, 24] (Supplementary Fig. 3c). The additional interfacing challenges for capturing element-level deformation and the additional computational requirements of the algorithm limit its use in dynamic deformation beam stabilization scenarios. In contrast to the state-of-the-art techniques, the DBS accomplishes the beam stabilization in a single unified framework that is: a) significantly less complex with no wireless back propagation link between the transmitter and the receiver, b) real-time model-free operation, c) significantly reduced memory storage as compared to the existing systems, and d) scalable with array elements unlike the element-level sensing.

Phase shift Resolution: The estimated phase code word (as in Eq. 1) can be written as :

$$\hat{P_\phi}[k+1] = \hat{P_\phi}[k] + A_I Y_{mul}[k] \tag{1}$$

where $\hat{P_\phi}[k+1]$ is the new estimation and $\hat{P_\phi}[k]$ is the previous estimation, A_I is the integrator gain and Y_{mul} is the multiplier output (see Fig. 8a in the main manuscript). If the phase shifter is continuous, when the phase code word approaches its optimum, the multiplier output gradually approaches to "zero" and the integrator output will be the previous value such that:

$$\hat{P_\phi}[k+1] = \hat{P_\phi}[k] + A_I Y_{mul}[k] \rightarrow \hat{P_\phi}[k+1] = \hat{P_\phi}[k] \tag{2}$$

If the phase shifter is discrete with a finite resolution ϕ_{res}, and the optimum phase shift ϕ_{opt} is between two discrete levels, then the gradient will not be zero and the loop will not settle to a final phase shift. Instead, it will dither the phase code word between the adjacent two code words $P_{\phi k}$ and $P_{\phi k+1}$, where $\phi_k < \phi_{opt} < \phi_{k+1}$. The error depends on the resolution of the phase shifter. For a 2-element array, the maximum error appears when ϕ_{opt} is exactly in the middle of $P_{\phi k}$ and $P_{\phi k+1}$. We can approximate the angular error $\theta_{err} = sin^{-1}(\frac{\phi_{res}}{2\pi})$. The phase shifter resolution of this work is 5°. Table Supplement2 shows the comparison with the state-of-the-art techniques. Our prior demonstration of a continuous-phase resolution beamforming [25] could be leveraged in future implementations.

Table Supplement2: Comparison with existing beam stabilization techniques.

Parameters	This Work	JSSC'21 [21]	TAP'23 [22]	IMS'21 [23]	TAP'13 [26]
Array Architecture	2x2 planar RX	20x20 planar TX	1x16 linear	8x1 TX/RX	1x4 linear
Array Processing	Active	Active	Passive	Active	Passive
Integration level	On-chip	On-chip	N/A	Discrete PCB	N/A
Building Blocks	RFFE, PS, Gain control, Beam stabilization	PLL, PA, Gain control, PS	N/A	PCB flex array, PS, PA, dig. control, Gain control, PLL	N/A
Antenna Fabrication	Additive Printed	Conventional Subtractive	Conventional Subtractive	Conventional Subtractive	Conventional Subtractive
Beam Stabilization (BS)	Silicon-based	FPGA-based (complex)	Micro-controller-based DNN	Mutual coupling matrix (desktop)	Strain sensor-based (mechanical)
Dynamic BS for Low SWaP-C	Scalable on-chip	Less scalable w/ complex over-the-air setup	Less scalable (apriori training)	Less scalable (off-chip)	Less scalable (off-chip)
Predetermined Deformation Insights	Not required	Not required	Required	Required[1]	Required[1]
Computation Complexity	O(3)	O(4) In parallel	O(5) In parallel	N/R	N/A
PS Resolution	5°	$\approx 1^\circ$	1.4° (COTS)	N/R	N/R
BS Power	$<3\ mW$	High power (FPGA)	High power (μC)	High power (PC)	N/R
BS Area	$<0.1\ mm^2$	FPGA	μC	PC	N/R

[1]Mutual coupling matrix under deformation; [2]In parallel; **RFFE** - RF Front End; **PLL** - Phase Locked Loop; **PA** - Power Amplifier; **DNN** - Deep Neural Network; **μC** - Micro-controller; **PC** - Desktop; Parallel processing, **PS** - Phase shifter; **N/A** - Not Applicable; **N/R** - Not Reported; **COTS** - Commercial off-the-shelf; **SWaP-C** - size, weight, area, power and cost

1.5 Non-uniform bending and multi-curvature surfaces

Multi-curvature bending is an example of non-uniform bending. As shown in Supplementary Fig. 4, the array is bent over two curvatures with radii R_1 and R_2 in opposite directions. The phase control code of antenna E_k is influenced by both R_1 and R_2. The optimal phase codeword is also affected by mutual coupling between

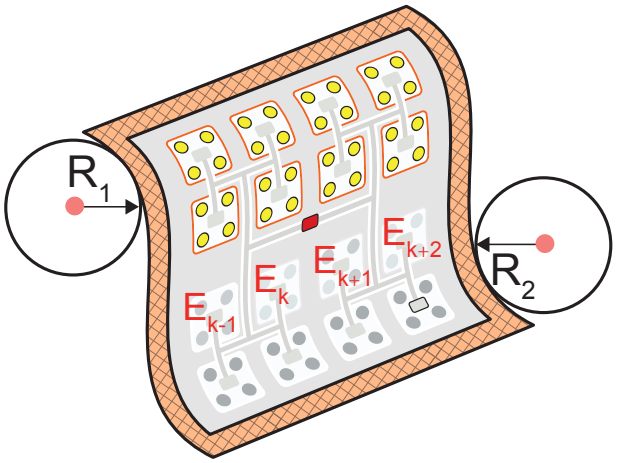

Supplementary Fig. 4 A non-uniform bending scenario.

all adjacent antennas. The mutual coupling from E_{k+1} and E_{k-1} is not straightforward, as both antennas are subject to the influence of R_1 and R_2. The perturbation amplitude for these elements plays a key role in the loop response under multicurvature bending. The perturbation amplitude has an upper bound beyond which the loop does not converge to the optimum phase, while very small perturbation amplitude can increase the convergence time. In this section, we will provide a theoretical framework for the DBS response under multi-curvature non-uniform bending. As explained before, the loop response of the deformation shown in Supplementary Fig. 4 cannot be explained using a single element approximation (a detailed single element DBS derivation provided in Supplementary 1.8). To understand the functionality of DBS in such cases, we consider an n-element DBS and assess its stability as it approaches the optimum point, given a DBS with input P_ϕ=$[P_{\phi 1}, P_{\phi 2}, ...P_{\phi n}]$, where P_ϕ is the phase code word for each element. Under the non-uniform bending scenario, all of the optimum phase code words $P_{\phi i}$ are independent of each other (assuming all elements are under the influence of more than one curvature). The system output is denoted as $BF_{out}(P_\phi)$. The perturbation to each phase code word can be written as $d_k = [A_1 sin(\omega k), A_2 sin(\omega k), ...A_n sin(\omega k)]$ where A_i is the perturbation amplitude of the i^{th} element and ω is the perturbation frequency. All perturbation frequencies are chosen to be the same and are generated from the same . The adaptive update rule for the multi-element DBS can be expressed as

$$P_{\phi k+1} = P_{\phi k} + G_k \partial_{P_\phi} f(\hat{P_\phi}) \tag{3}$$

where $\partial_{P_\phi} f(\hat{P_\phi})$ is the gradient and G_k is a scale factor dependent on the HPF, multiplier, and integrator gain. Using the averaged model explained in [27], after applying perturbation d_k and multiplication, the average dynamics of $P_{\phi k}$ in steady state can be expressed as: (please note that in the rest of this section ∂ represents partial derivation with respect to phase code word ∂_{P_ϕ})

$$\hat{P}_{\phi k+1} = \hat{P_{\phi k}} - \gamma diag(A^2) \partial f(P_\phi) \tag{4}$$

where γ is the step size or learning rate, $\hat{P_{\phi k}}$ is slowly varying component of $P_{\phi k}$ averaged over time and $diag(A^2)$ is a diagonal vector with perturbation amplitudes.

$$diag(A^2) = \begin{bmatrix} A_1^2 & 0 & ... & 0 \\ 0 & A_2^2 & ... & 0 \\ . & . & & . \\ . & . & & . \\ 0 & 0 & ... & A_n^2 \end{bmatrix} \tag{5}$$

When the array undergoes dynamic, non-uniform bending, the DBS must determine the optimal phase code words ($P^*_{\phi k}$) that correspond to the optimal beamforming output $BF_{out,opt}$. Under a specific bending condition, there exists only one maximum $BF_{out,opt}$ which corresponds to a unique set of $P_{\phi k}$. To assess the capability of the DBS in finding this unique $P_{\phi k}$, we need to analyze its stability under the assumption that all phase code words are completely independent. Stability can be evaluated by considering the beamforming function at the optimum point and examining the eigenvalues of the transition matrix.

At the optimal phase code word $P^*_{\phi k}$ gradient is '0', i.e., $\partial BF_{out}(P^*_{\phi k}) = 0$. We linearize the beamforming function around the optimum point to analyze stability. We can define the deviation from the optimum point as follows. $\delta P_{\phi k} = P_{\phi k} - P^*_{\phi k}$. Using first-order Taylor series expansion, we can express

$$\partial BF_{out}(P_{\phi k}) = BF_{out}(P^*_{\phi k}) + H({P_\phi}^*)(P_\phi - {P_\phi}^*) \tag{6}$$

where $H({P_\phi}^*)$ is the Hessian matrix of $BF_{out}(P_{\phi k})$ at ${P_\phi}^*$, and $BF_{out}(P^*_{\phi k}) = 0$. Substituting the Taylor series approximation (Eq. 6) in Eq. 4, the averaged model can be rewritten as:

$$\hat{P_{\phi k+1}} = \hat{P_{\phi k}} - \gamma diag(A^2) H({\hat{P}_\phi}^*)(\hat{P_\phi} - {\hat{P}_\phi}^*) \tag{7}$$

This can be expressed in terms of deviation δ_k:

$$\delta_{P_{\phi k+1}} = \delta_{P_{\phi k}} - \gamma diag(A^2) H({\hat{P}_\phi}^*) \delta_{P_\phi} \tag{8}$$

and the linearized dynamics can be written as

$$\delta_{P_{\phi k+1}} = [I - \gamma diag(A^2) H({\hat{P}_\phi}^*)] \delta_{P_\phi} \tag{9}$$

where I is the identity matrix, and the second term is the feedback. We can call this a transition matrix M

$$M = I - \gamma diag(A^2) H({\hat{P}_\phi}^*) \tag{10}$$

The DBS is stable if the deviations $\delta_{P_{\phi k}}$ decay to zero over time which means the eigenvalues $\lambda_i(M)$ of transition matrix M satisfies the following condition

$$|\lambda_i(M)| < 1 \tag{11}$$

The eigenvalues of M can be written as

$$\lambda_i(M) = 1 - \gamma A_i \lambda_i(H) \tag{12}$$

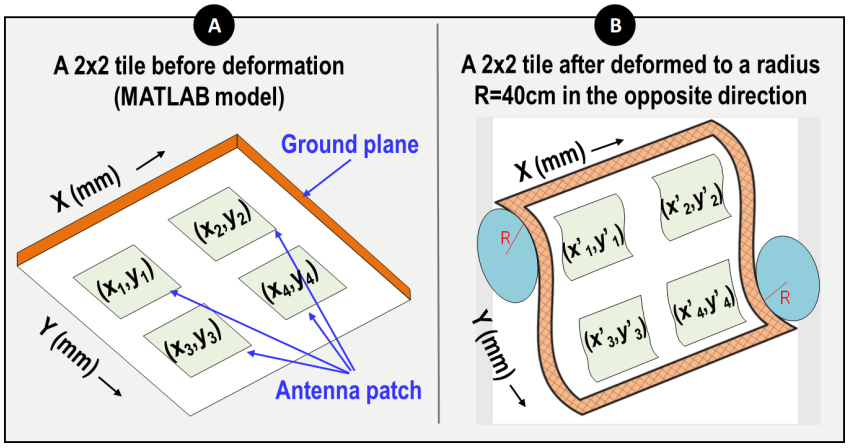

Supplementary Fig. 5 Simulation model for multi curvature bending: **a.** 2×2 planar patch antenna array before deformation. **b.** Array deformed over a curvature R = 40 cm in opposite directions.

From Eq. 11 we can derive the stability conditions as follows

$$1 - \gamma A_i \lambda_i(H) > -1 \tag{13}$$

$$1 - \gamma A_i \lambda_i(H) < 1 \tag{14}$$

which can be summarized together as :

$$0 < \gamma A_i \lambda_i(H) < 2 \tag{15}$$

This implies that the perturbation amplitudes must be carefully selected to ensure the DBS stability. In environments where the array is susceptible to non-uniform, multi-curvature bending, the perturbation amplitudes should be chosen as described in Eq. 15. As the perturbation amplitude increases, the speed of the loop increases, but when it goes beyond a particular amplitude, the loop does not converge. To validate this theoretical framework, we have conducted MATLAB simulations with a multi-curvature array and DBS as illustrated in Supplementary Fig. 5. The initial position of each element of the 2 × 2 tiles is shown in Supplementary Fig. 5a. Now the planar array shown in Supplementary Fig. 5a is deformed with radius R (= 40 cm) in opposite directions. The new (X,Y,Z) dimensions of each element are estimated under deformation. Based on the new positions array steering vector is estimated using the phased array toolbox in MATLAB and fed to the DBS algorithm implemented in MATLAB. The final positions after deformation are shown in Supplementary Fig. 5b. After updating the element positions, the array gain is simulated using the antenna array toolbox in MATLAB and optimized to its maximum, assuming a continuous time phase shifter. The simulated results for the curvature in Supplementary Fig. 5b are shown in Supplementary Fig. 6. The perturbation amplitude is chosen as $A_\phi = 0.1$, which is well below the condition shown in Eq. 15.

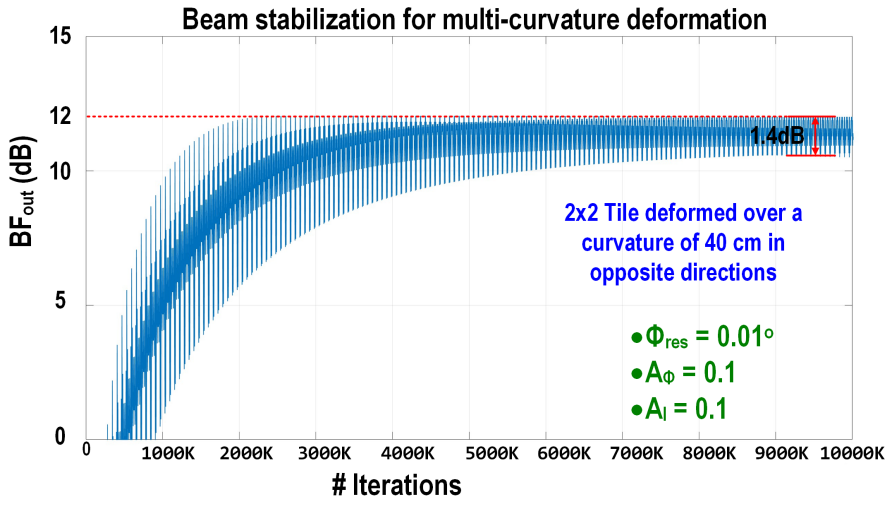

Supplementary Fig. 6 Simulated results for the curvature in Fig. 5b. The convergence speed is low because the simulation uses (i) a continuous phase shifter for generality, (ii) a perturbation amplitude of $a_\phi = 0.01$ to satisfy Eq. 15, and (iii) the DBS initializes with worst-case phase shifts.

1.6 Impacts of Ink Resistivity Variations

This section illustrates the impact of resistivity variations on the RF properties of the array.

1.6.1 Variation in S_{11}

We analyze the impact of printing imperfections and variations in ink resistivity on the substrate impedance, particularly affecting the antenna input impedance and the characteristic impedance of the RF lines.

Since temperature and strain variations are the main reasons behind resistivity changes and impedance mismatches, we now also experimentally verify the impedance variations on proposed ink-based RF lines. Consider the characteristic impedance (Z_O) of an RF trace as follows [28]:

$$Z_0 = \sqrt{\frac{j\omega L + R}{j\omega C + G}} \tag{16}$$

Compared to bulk copper, printed ink has higher resistance R and lower conductance G, so the small fractional variations in resistivity will have an adverse effect on the characteristic impedance. The input impedance of an RF trace can be written as:

$$Z_{in} = Z_0 \frac{Z_L + Z_0 tanh\gamma_{TL} l}{Z_0 + Z_L tanh\gamma_{TL} l} \tag{17}$$

where γ_{TL} is the propagation constant, which can be defined as:

$$\gamma_{TL} = \alpha + j\beta = \sqrt{(R + j\omega L)(G + j\omega C)} \tag{18}$$

Assuming a lossless trace, the characteristic impedance of the trace is: $Z_o = \sqrt{L/C}$. For a lossless transmission, we can rewrite the propagation constant as:

$$\gamma_{TL} \approx j\beta + \frac{R}{2Z_o} + \frac{GZ_o}{2} \tag{19}$$

Equation 17 can be further expressed in terms of trace resistance and conductance as:

$$Z_{in} = Z_0 \frac{Z_L + jZ_0 tan(\beta l) + j\frac{R/Z_o + GZ_o}{2} l}{Z_0 + Z_L tan(\beta l) + j\frac{R/Z_o + GZ_o}{2} l} \tag{20}$$

The return loss, S_{11}, can further be defined as:

$$S_{11} = 20log\left|\frac{Z_{in} - Z_0}{Z_0 + Z_{in}}\right| \tag{21}$$

It can be inferred from Eq 16-21, considering a lossless line, that the trace return loss (S_{11}) significantly depends on its resistance (R) and conductance (G). Strain or temperature variations can alter the return loss. Especially, in the case of non-uniform or multi-curvature bending, the strain at each point of the array varies, leading to significant impedance mismatches. This impedance mismatch causes signal reflections, manifesting as loss in the signal power.

Due to the S_{11} variations, these printed antennas are often used as strain and temperature sensors by printing on materials that exacerbate these variations. As shown in [29], a patch operating at 3.7 GHz screen printed using silver ink shows ≈ 20 dB variation in S_{11} over 3.5% strain. Similarly, a dual-band loop antenna, resonating at both 1.2 GHz and 5.8 GHz, printed on PVC using silver, shows a 3.5 dB change in S_{11} over temperature change from 25° to 90° [30]. For applications such as DBS-FLEX, it is important to verify that the resistivity variations of the ink are minimal.

1.6.2 Variation in Phase constant β

The propagation constant of a transmission line can be expressed as

$$\gamma = \alpha + j\beta \tag{22}$$

where α represents the attenuation through the traces (transmission line) and β is the phase constant that represents the phase of the signal traveling through the traces. The phase constant can be expressed as

$$\beta = \sqrt{(j\omega L + R)(j\omega C + G)} \tag{23}$$

For an ideal lossless line, R is zero and G is infinite. and the phase constant only depends on the L and C. For additive printed traces, the R and G values are far from ideal values due to their increased resistivity. Therefore, the phase constant variations can affect the overall array.

1.7 Simulated Annealing based DBS

For the current implementation of DBS, the optimization loop can occasionally get stuck in a local maximum. Although the presented 2×2 implementation exhibits only weak local maxima (sidelobes) in its beam pattern (as shown in Fig. 5c and Fig. 5d), increasing the array size leads to more prominent sidelobes that can act as local maxima alongside the main lobe. To address this limitation and ensure that the optimized phase configuration corresponds to the global maximum, a global search can be employed. Supplementary Figure 7 presents a simulation in which a global search is performed by the simulated annealing technique after DBS has converged to its initial optimum. For simplicity, a continuous-time phase shifter is used, and a 4×1 uniform linear array is assumed to ensure sufficient sidelobe formation. It was observed that, with the current simulation settings, DBS typically converges within 50 iterations. Therefore, a global search is triggered after every 50 iterations. Despite the presence of local maxima, this strategy consistently guides the loop to the global maximum. Rather than choosing a fixed number of iterations, an adaptive strategy can be employed: the beamformer output (BF_{out}) can be compared to the output of a single antenna element. If $BF_{\text{out}} < 20\log(N_x N_y/2)$, this may indicate that the system is trapped in a local maximum. In such cases, a global search using simulated annealing can be initiated. For an $N_x \times N_y$ array, when all signals are perfectly aligned, the beamforming gain is $20\log(N_x N_y)$.

1.8 DBS Operation

We step through each stage to understand the DBS functionality in detail. As shown in Fig 8a, ① on- chip look-up table (LUT) generate sinusoidal perturbation $sin[\omega k]$ which is amplified by a_ϕ. This will perturb the phase code word around $P_{\phi A}$ as shown in ②.

$$P_\phi[k] = P_{\phi A} + a_\phi sin[\omega k] \tag{24}$$

Due to the dynamic change at t=T_1, the BF_{out} falls from $BF_{out,opt}$ to $BF_{\text{out},1}$ as shown by ③. The corresponding change in BF_{out} is captured by passing it through the high-pass filter (HPF),

$$Y_{\text{HPF}}[k] = aY_{\text{HPF}}[k-1] + BF_{\text{out}}[k] - BF_{\text{out}}[k-1] \tag{25}$$

where HPF is expressed as $\frac{1-z^{-1}}{1-az^{-1}}$ with a depending on the cut-off frequency. The captured variations are then multiplied by the initial perturbation as shown in ④,

$$Y_{mul}[k] = Y_{HPF}[k]a_\phi sin[\omega k] \tag{26}$$

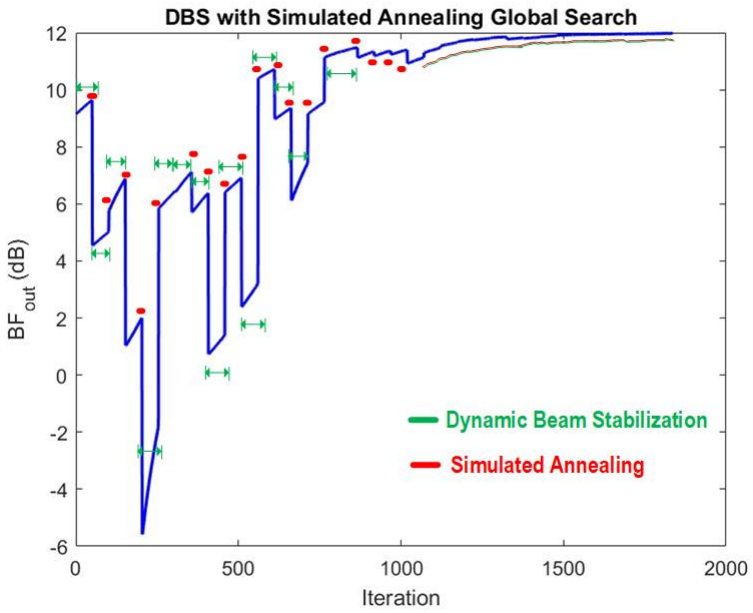

Supplementary Fig. 7 Simulated results of DBS with a simulated annealing global search. A uniform linear array with a continuous time phase shifter is considered for the simulation.

The subsequent integrator can be simplified as a zero-order-hold integrator, expressed as I(z)=$A_{\mathrm{I}}/(1-z^{-1})$, where A_{I} is the integrator gain. The integrator output estimates the new step size as shown in Fig. 8b and is expressed as:

$$\hat{P_\phi}[k+1] = \hat{P_\phi}[k] + A_I Y_{mul}[k] \tag{27}$$

The $\hat{P_\phi}[k+1]$ is the new estimation, and $A_I Y_{mul}(k)$ is the new step size (shown as α). The $\hat{P_\phi}[k+1]$ is added with the LUT as shown in ②, and the process is repeated. α will be auto updated based on the multiplier output Y_{mul} until it reaches $P_{\phi B}$. The integrator output is then summed with the LUT perturbation and fed back to the BFIC. The adaptive update can be simplified as:

$$P_\phi[k+1] = \hat{P_\phi}[k+1] + a_\phi sin[\omega[k+1]] \tag{28}$$

Next, we will see how DBS estimates the gradient with array-level information without any element-level information.

The phase-shifter code word $P_\phi[k]$ can be expressed as:

$$P_\phi[k] = \hat{P_\phi}[k] + a_\phi sin[\omega k] \tag{29}$$

where $\hat{P_\phi}$ is the estimated phase code-word after each iteration, a_ϕ is the perturbation amplitude and ω is the perturbation frequency. Expressing $\mathrm{BF_{out}}$ as a function of this phase-shifter code-word as follows:

$$BF_{out}[k] = f(P_\phi[k]) = f(\hat{P_\phi}[k] + a_\phi sin[\omega k]) \tag{30}$$

The first-degree Taylor series expansion of a function $f(x)$ around a can be expressed as $f_a(x) = f(a) + \partial_x f(a)(x-a)$, where ∂ is the partial-differential operated on the estimated phase-shifter code-word. The BF_{out} can be expressed as Taylor series expansion around $\hat{P_\phi}$ as follows:

$$\begin{aligned} BF_{out\hat{P_\phi}}[P_\phi] &= BF_{out}[\hat{P_\phi}] + \partial_{P_\phi} BF_{out}[\hat{P_\phi}] \cdot [P_\phi - \hat{P_\phi}] \\ &= BF_{out}[\hat{P_\phi}] + \partial_{P_\phi} BF_{out}[\hat{P_\phi}] \cdot [\hat{P_\phi} + a_\phi sin[\omega k] - \hat{P_\phi}] \\ &= BF_{out}[\hat{P_\phi}] + \partial_{P_\phi} BF_{out}[\hat{P_\phi}] \cdot [a_\phi sin[\omega k]] \end{aligned} \tag{31}$$

The first term in (31) is a DC term, while the second term represents a sinusoidal variation in BF_{out} resulting in the perturbation in the phase code word. It is straightforward to use a HPF to extract the time-varying term, which contains the gradient information.

$$Y_{HPF}[k] = \partial_{P_\phi} BF_{out}[\hat{P_\phi}](A_{HPF} \cdot a_\phi sin[\omega k + \Omega_{HPF}]) \tag{32}$$

where A_{HPF} and Ω_{HPF} are the magnitude and phase changes due to HPF. The filter cut-off frequency is chosen such that this term is minimally distorted. The HPF output is now multiplied by the LUT perturbation as follows:

$$\begin{aligned} Y_{mul}[K] &= a_\phi sin[\omega k] \cdot \partial_{P_\phi} BF_{out}[\hat{P_\phi}] \cdot (A_{HPF} \cdot a_\phi sin[\omega k + \Omega_{HPF}]) \\ &= a_\phi^2 A_{HPF} \cdot sin[\omega k] \cdot (sin[\omega k + \Omega_{HPF}]) \cdot \partial_{P_\phi} BF_{out}[\hat{P_\phi}] \\ &= X[k] \partial_{P_\phi} BF_{out}[\hat{P_\phi}] \end{aligned} \tag{33}$$

where $X[k]$ is the time-varying factor. The multiplier output as shown in Eq. 33 contains gradient information of $BF_{out}[P_\phi]$ at $\hat{P_\phi}$. The subsequent integrator can be simplified as a zero-order hold integrator, expressed as $\mathrm{I(z)}=A_I/(\mathrm{z}-1)$, where A_I is the integrator gain. The integrator output can be expressed as:

$$\hat{P_\phi}[k+1] = \hat{P_\phi}[k] + A_I Y_{mul}[k] \tag{34}$$

where $\alpha = A_I Y_{mul}[k]$ at $\hat{P_\phi}$ is the new step size as shown in Fig. 8b.

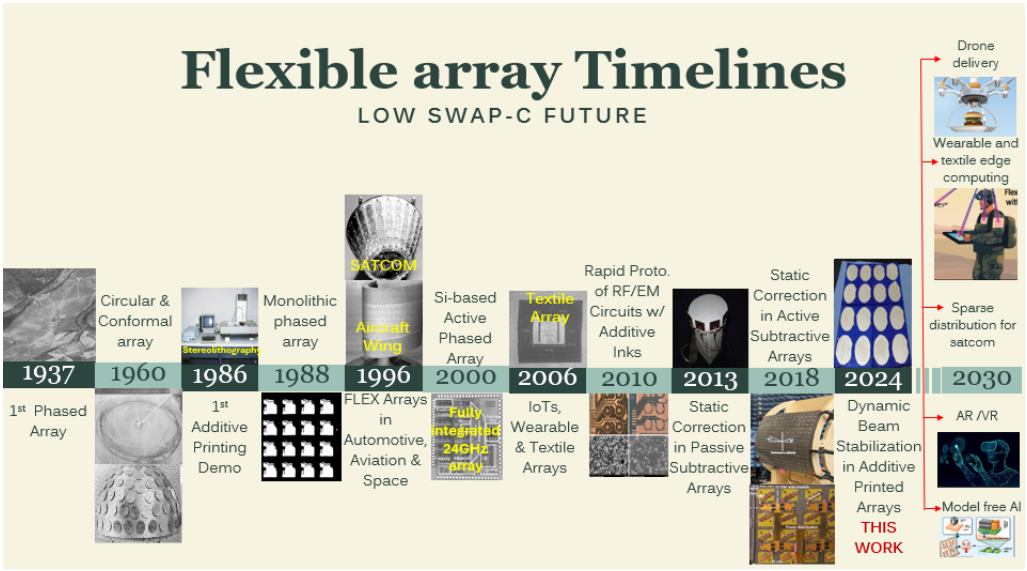

Supplementary Fig. 8 Historical timelines showing the evolution of low SWaP-C flexible arrays with future evolution into fast insight generation at the edge to provide long endurance flight for long hours.

2 Additional pictures

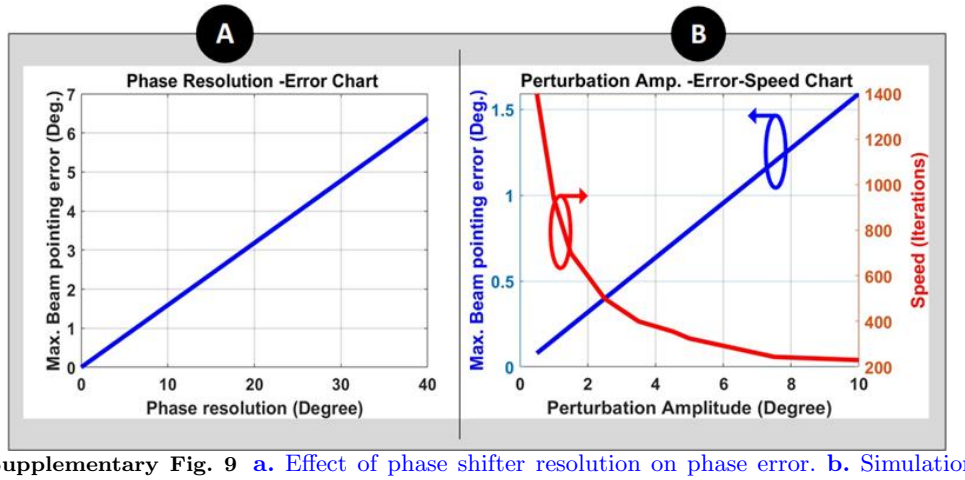

Supplementary Fig. 9 **a.** Effect of phase shifter resolution on phase error. **b.** Simulation results showing the effect of perturbation amplitude on beam pointing error and convergence speed.

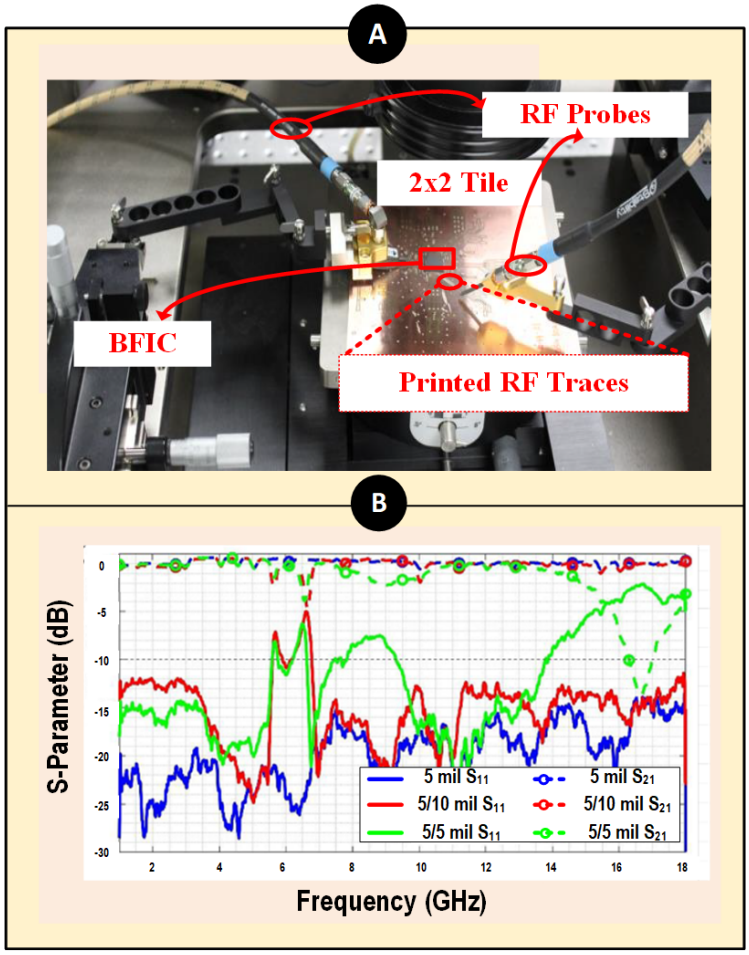

Supplementary Fig. 10 Measurement of the insertion loss of the RF traces **a.** Probe station setup for measuring the S_{21}. **b.** Measured S_{21} showing negligible insertion loss at the desired frequency of interest (2.1GHz).

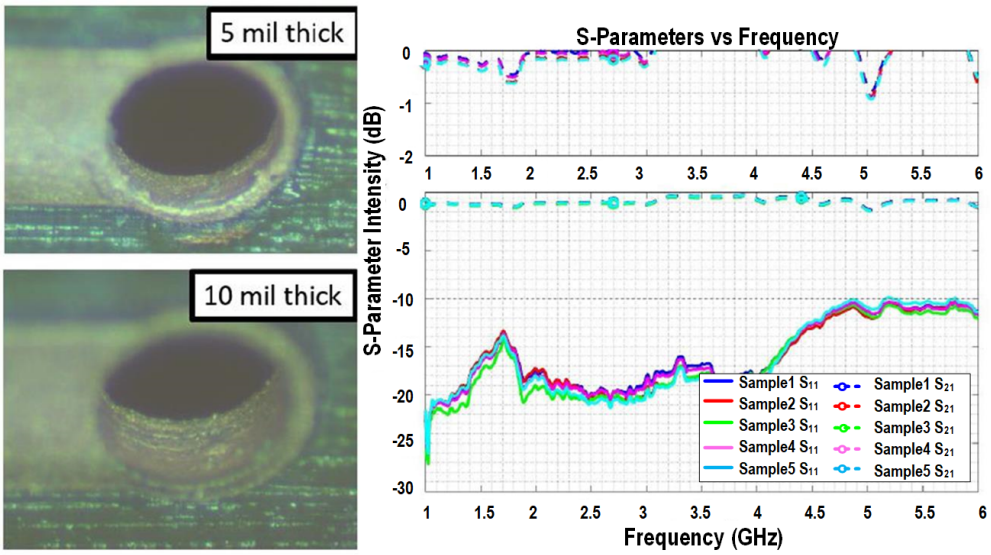

Supplementary Fig. 11 Measured losses in the additive printed vias for two different via thickness

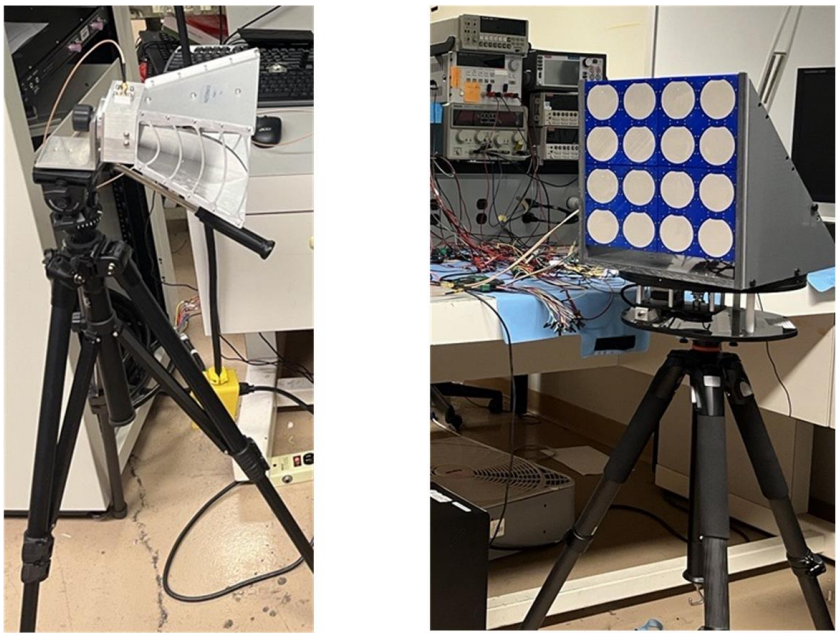

Supplementary Fig. 12 Measurement setup for over-the-air testing. The horn antenna (left) transmits the modulated beam to the multi-antenna BFIC (right) with self-beam stabilization.

Supplementary Fig. 13 Proposed copper molecular decomposition inks at different stages of preparation: Screen-Printed ink verifying its viscosity and printability, Sintered and ball-milled ink.

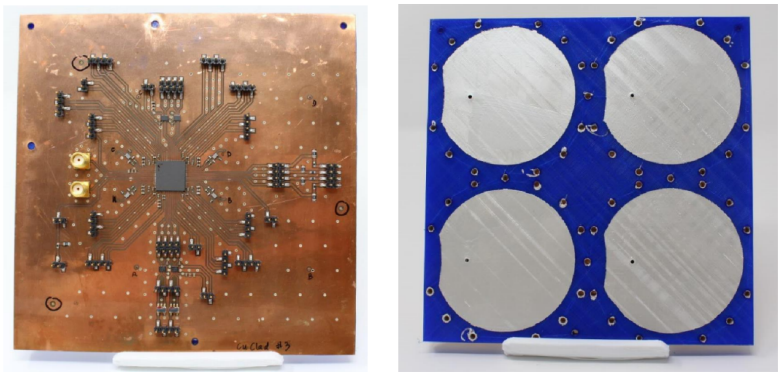

Supplementary Fig. 14 2×2 tile back and front sides after fabrication.

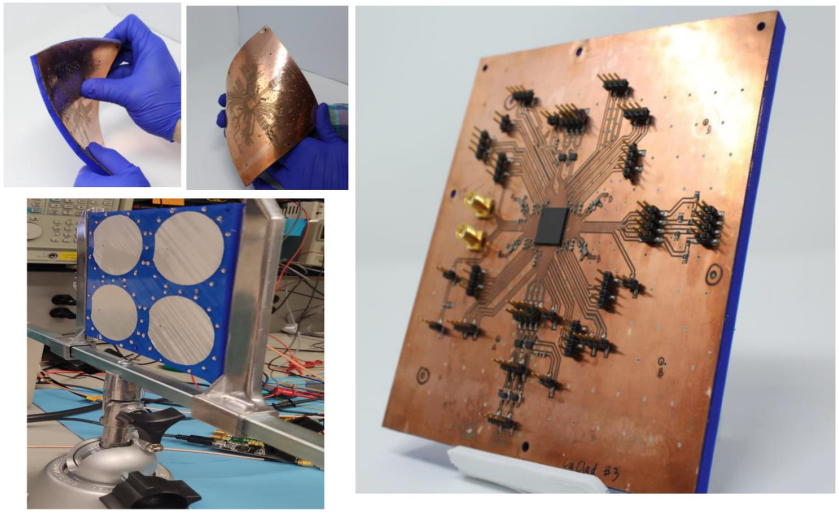

Supplementary Fig. 15 2×2 tile at various stages.

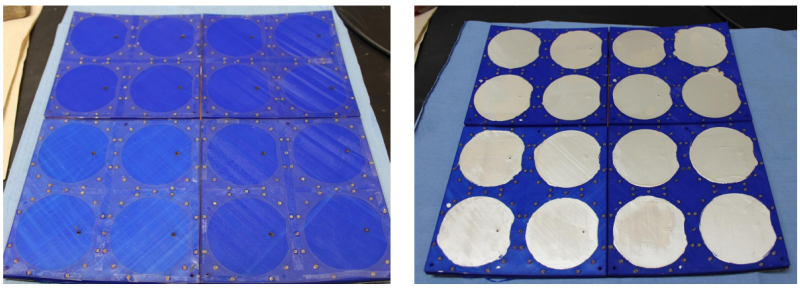

Supplementary Fig. 16 Construction of four 2×2 arrays tiled to form 4×4 array (bonding with BFIC not shown).

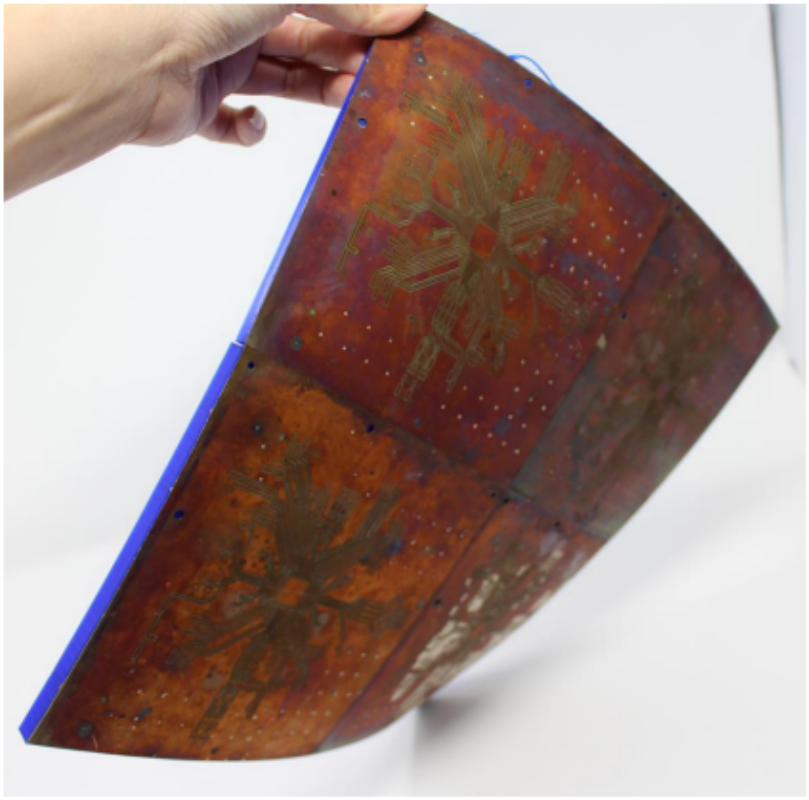

Supplementary Fig. 17 4×4 arrays before attaching BFIC and its connections.

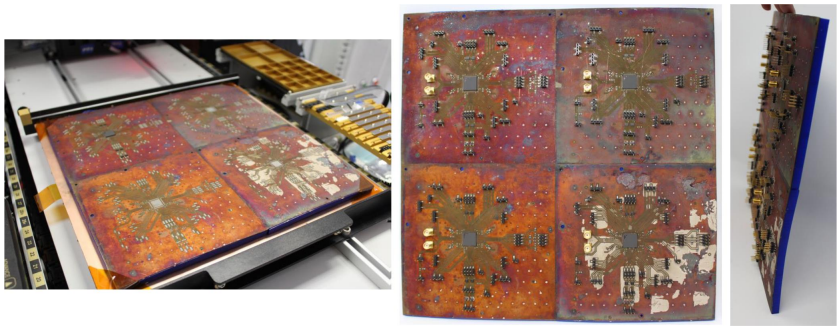

Supplementary Fig. 18 Ultra-low temperature soldering for 4×4 to accommodate Ninjaflex melting point. 4×4 arrays after attaching BFIC and its connections.

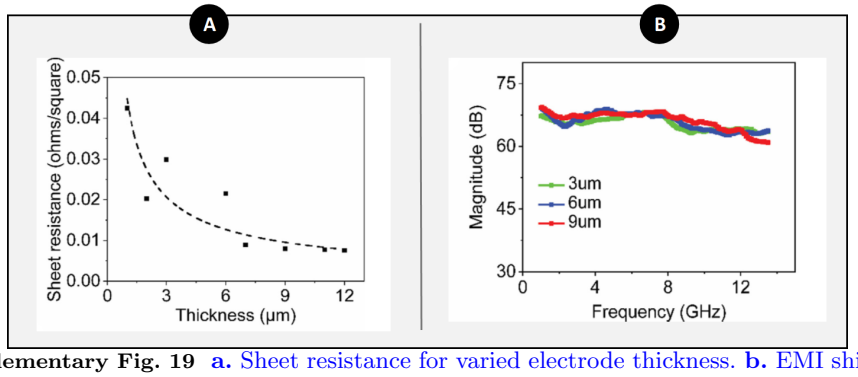

Supplementary Fig. 19 **a.** Sheet resistance for varied electrode thickness. **b.** EMI shielding performance at different sample thickness.

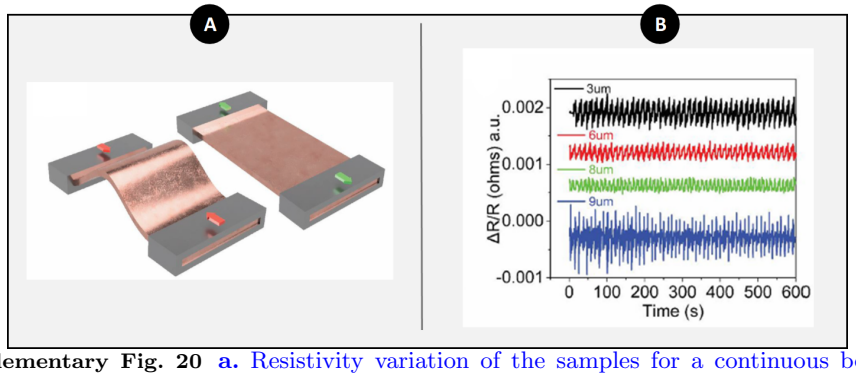

Supplementary Fig. 20 **a.** Resistivity variation of the samples for a continuous bending cycle of 10 mins. **b.** Schematic depiction of bend test apparatus.

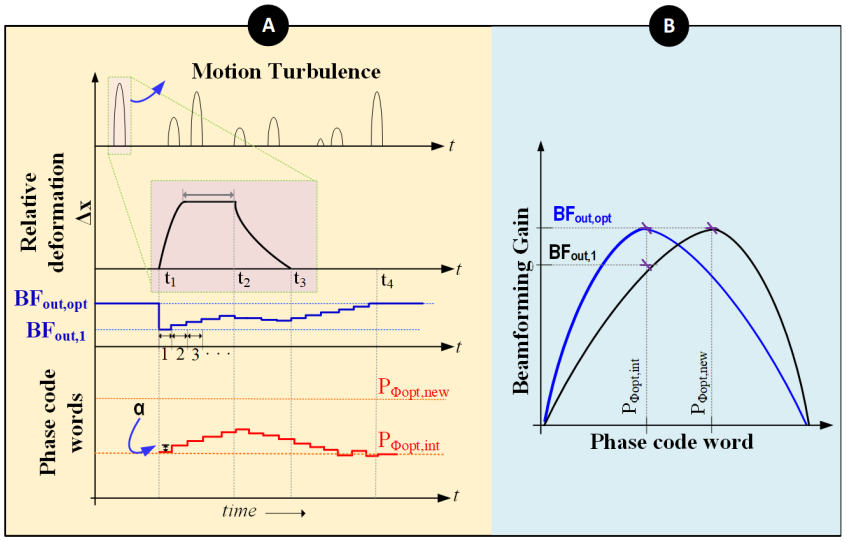

Supplementary Fig. 21 A short transient deforming the array. **a.** DBS response in time domain. **b.** Beamforming gain change due to turbulence.

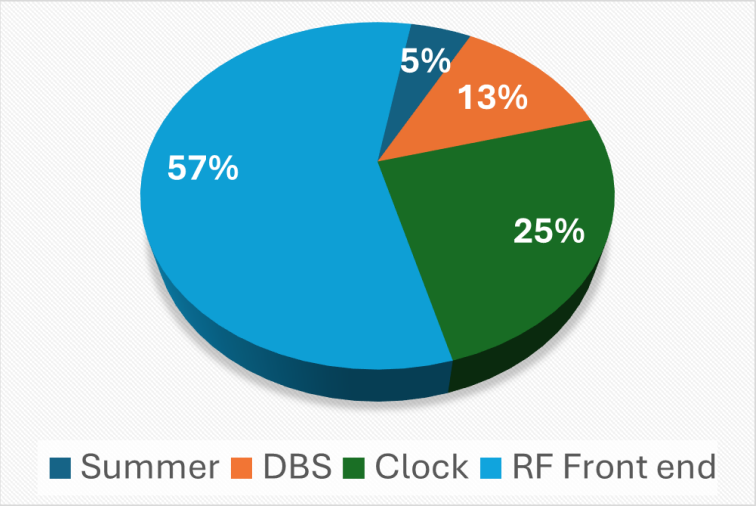

Supplementary Fig. 22 Power breakdown of the proposed DBS-FLEX array.

Excitation ($P_{\phi n}$)	Response (BF_{out})	Loop Status
$P_{\phi n}+K$, $P_{\phi n}$, $P_{\phi n}-K$	$BF_{out,opt}$	Increasing phase increases BF_{out}. Optimum phase is higher than ϕ_n
$P_{\phi n}+K$, $P_{\phi n}$, $P_{\phi n}-K$	$BF_{out,opt}$	Increasing phase decreases BF_{out}. Optimum phase is lower than ϕ_n
$P_{\phi n}+K$, $P_{\phi n}$, $P_{\phi n}-K$	$BF_{out,opt}$	Loop settled to its maxima. $P_{\phi n}$ is the optimum phase code word and ϕ_n is the optimum phase

Supplementary Fig. 23 Table illustrating DBS operation.

References

[1] Get started with power automate (Nov. 15, 2023) https://learn.microsoft.com/en-us/power-automate/getting-started

[2] Bieri, N., *et al.*: Gold nanoparticle-based electronics. Appl. Phys. Lett. **82**(20), 3529 (2003)

[3] Critchley, K., *et al.*: Self-assembled gold nanowires. Nat. Chem. **12**(2), 1031–1036 (2010)

[4] Kramer, R.K., *et al.*: Liquid metal electronics: A review. Langmuir **30**(2), 533 (2014)

[5] Wang, L., Liu, J.: Room-temperature liquid metals for flexible electronics. Imaging Sci. Photochem **32**, 382 (2014)

[6] Mo, L., *et al.*: Silver nanoparticle ink for printable electronics. Appl. Surf. Sci. **257**(13), 5746 (2011)

[7] Sharipov, M., *et al.*: Conductive silver nanoparticle inks. Mater. Adv. **2**(11), 3579 (2021)

[8] Gu, W., *et al.*: Nanostructured silver inks for printed electronics. RSC Adv. **8**(53), 30215 (2018)

[9] Park, K., *et al.*: Stabilization of silver nanoparticles in conductive inks. Colloids Surf. A **313**, 351 (2008)

[10] Chen, J.-J., *et al.*: High-conductivity silver nanowire networks. Mater. Des. **154**, 266 (2018)

[11] Kumar, A., *et al.*: Printable agnw inks for flexible electronics. Nanomaterials **11**(3), 693 (2021)

[12] Park, B.K., *et al.*: Inkjet printed copper nanoparticle ink. Thin Solid Films **515**(19), 7706 (2007)

[13] Lee, Y., *et al.*: Stable copper nanoinks for printed electronics. Nanotechnology **19**(41), 415604 (2008)

[14] Li, W., *et al.*: Oxidation-resistant copper nanoparticles. Mater. Chem. Phys. **146**(1–2), 82 (2014)

[15] Liu, J., *et al.*: Copper nanomaterials for electronic devices. J. Mater. Sci.: Mater. Electron. **27**, 13280 (2016)

[16] Arbab, A.A., *et al.*: Flexible carbon-based conductive films. J. Colloid Interface

Sci. **539**, 95 (2019)

[17] Pidcock, G.C., Panhuis, M.: Flexible electronics using cnt networks. Adv. Funct. Mater. **22**(22), 4790 (2012)

[18] Huang, X., *et al.*: High-performance graphene films for electronics. 2D Mater. **3**(2), 025021 (2016)

[19] Nitta, K., *et al.*: Pedot:pss conductive polymers. J. Phys. D: Appl. Phys. **52**(31), 315202 (2019)

[20] Ngamna, O., *et al.*: Flexible polyaniline conductive films. Langmuir **23**(16), 8569 (2007)

[21] Hajimiri, A., *et al.*: Dynamic focusing of large arrays for wireless power transfer and beyond. IEEE Journal of Solid-State Circuits **56**(7), 2077–2101 (2021) https://doi.org/10.1109/JSSC.2020.3036895

[22] Cao, K., *et al.*: Beam stabilization of deformed conformal array antenna based on physical- method -driven deep learning. IEEE Transactions on Antennas and Propagation **71**(5), 4115–4127 (2023) https://doi.org/10.1109/TAP.2023.3249348

[23] Mizrahi, O.S., Fikes, A., Hajimiri, A.: Flexible phased array shape reconstruction. In: 2021 IEEE MTT-S International Microwave Symposium (IMS), pp. 31–33 (2021). https://doi.org/10.1109/IMS19712.2021.9574941

[24] Fikes, A., Mizrahi, O.S., Hajimiri, A.: A framework for array shape reconstruction through mutual coupling. IEEE Transactions on Microwave Theory and Techniques **69**(10), 4422–4436 (2021) https://doi.org/10.1109/TMTT.2021.3097729

[25] Slater, A., Abbasi, H., Poolakkal, S., Beheshti, F., Gupta, S.: Enhancing continuous beam angle resolution for next generation wireless systems: A multi-stage phase-shifting polyphase filters approach. IEEE Transactions on Circuits and Systems I: Regular Papers **71**(11), 5200–5210 (2024) https://doi.org/10.1109/TCSI.2024.3425861

[26] Braaten, B.D., *et al.*: A self-adapting flexible (selflex) antenna array for changing conformal surface applications. IEEE Transactions on Antennas and Propagation **61**(2), 655–665 (2013) https://doi.org/10.1109/TAP.2012.2226227

[27] Rotea, M.A.: Analysis of multivariable extremum seeking algorithms. In: Proceedings of the 2000 American Control Conference. ACC (IEEE Cat. No.00CH36334), vol. 1, pp. 433–4371 (2000). https://doi.org/10.1109/ACC.2000.878937

[28] Pozar, D.M.: Microwave Engineering. Wiley, Fourth Edition (2011)

[29] Jeong, H., Lim, S.: A stretchable radio-frequency strain sensor using screen printing technology. Sensors (Basel) **16**(11), 1839 (2016) https://doi.org/10.3390/s16111839. . PMID: 32202762

[30] Bhattacharjee, M., Nikbakhtnasrabadi, F., Dahiya, R.: Printed chipless antenna as flexible temperature sensor. IEEE Internet of Things Journal **8**(6), 5101–5110 (2021) https://doi.org/10.1109/JIOT.2021.3051467